



Original Article

High resolution size characterization of particulate contaminants for radioactive metal waste treatment

Min-Ho Lee¹, Wonseok Yang¹, Nakkyu Chae, Sungyeol Choi^{*}

Korea Advanced Institute of Science and Technology, Department of Nuclear and Quantum Engineering, 291 Daehak-ro, Yuseong-gu, Daejeon, 34141, Republic of Korea

ARTICLE INFO

Article history:

Received 22 July 2020

Received in revised form

14 January 2021

Accepted 25 January 2021

Available online 2 February 2021

Keywords:

Radioactive aerosols

Decommissioning

Plasma arc cutting

Aerodynamic diameter

HR-ELPI⁺

ABSTRACT

To regulate the safety protocols in nuclear facilities, radioactive aerosols have been extensively researched to understand their health impacts. However, most measured particle-size distributions remain at low resolutions, with the particle sizes ranging from nanometer to micrometer. This study combines the high-resolution detection of 500 size classes, ranging from 6 nm to 10 μm , for aerodynamic diameter distributions, with a regional lung deposition calculation. We applied the new approach to characterize particle-size distributions of aerosols generated during the plasma arc cutting of simulated non-radioactive steel alloy wastes. The high-resolution measured data were used to calculate the deposition ratios of the aerosols in different lung regions. The deposition ratios in the alveolar sacs contained the dominant particle sizes ranging from 0.01 to 0.1 μm . We determined the distribution of various metals using different vapor pressures of the alloying components and analyzed the uncertainties of lung deposition calculations using the low-resolution aerodynamic diameter data simultaneously. In high-resolution data, the changes in aerosols that can penetrate the blood system were better captured, correcting their potential risks by a maximum of 42%. The combined calculations can aid the enhancement of high-resolution measuring equipment to effectively manage radiation safety in nuclear facilities.

© 2021 Korean Nuclear Society, Published by Elsevier Korea LLC. This is an open access article under the CC BY-NC-ND license (<http://creativecommons.org/licenses/by-nc-nd/4.0/>).

1. Introduction

Radioactive aerosols, ranging from nano-to micro-sized particles, are produced during severe accidents in nuclear power plants or decommissioning of nuclear facilities [1,2]. During the treatments of contaminated materials, cutting surface-contaminated and neutron-activated radioactive materials is unavoidable [3–5], which generates radioactive aerosols, with sizes ranging from a few nanometers to tens of micrometers [6–8]. These generated aerosols contribute to surface contamination in the workplace and subject the workers and public to internal radiation exposure [6,9,10]. The deposition of the inhaled aerosols on the respiratory tracts can be determined using several parameters, such as the particle sizes of the aerosols, respiratory airways, and breathing conditions [11]. Most previous studies determined the characterization of aerosols in a low resolution with 15–20 size classes, ranging from a few

nanometers to micrometers [12–21]. However, to calculate the deposition ratios accurately and interpret the consequences of the radioactive aerosols precisely, the aerodynamic diameter distributions of the aerosols must be determined using high-resolution detection. By quantitatively comparing the computations of low-resolution data with high-resolution data, this study identified the importance of high-resolution detection for the safety assessment of nuclear decommissioning.

The radioactive aerosols generated during the cutting of activated metals can affect the internal organs and penetrate the blood systems. Therefore, a thorough understanding of the radiological hazard and toxic effects of the metallic particles is essential. Thus far, the health effects of the ambient particulate matter (PM) have been studied extensively [22–27]. Considering the aerodynamic diameter, PMs are classified into three categories, i.e., PM₁₀, PM_{2.5}, and PM_{0.1}, representing the classes of inhalable coarse particles, fine particles (fine dust), and ultra-fine particles with a diameter smaller than 10, 2.5, and 0.1 μm , respectively. PM_{2.5} and PM_{0.1} easily enter the pulmonary alveoli, wherein gas exchange occurs across the biological tissues [22]. Additionally, PM_{2.5} or smaller particles

^{*} Corresponding author.

E-mail address: sungyeolchoi@kaist.ac.kr (S. Choi).

¹ Both authors contributed equally.

penetrate the blood circulation system through the lung cells [26,27]. Inhaling these particles incorporated with radioactive isotopes causes breathing problems, damages respiratory organs, and accumulates radiation doses in the tissues.

Plasma arc cutting rapidly treats the thick and conductive radioactive materials such as aluminum, steel, and nickel alloys that are commonly used in the nuclear industry [28–30]. This method generates a plasma at a typical temperature of 28,000 °C [6,21,31] and aerosol particles incorporated with radioactive isotopes under extreme environments. Furthermore, the vaporized molten metals form volatile oxides that explode into metallic droplets or gas bubbles. Unlike plasma arc welding [32–50], the awareness of the physio-chemical characteristics and health impacts of the radioactive aerosols generated during plasma arc cutting is limited [6–8,18]. Therefore, a deeper insight into the fine particle distribution can provide an accurate interpretation of the health impacts of these aerosol particles.

Therefore, this study analyzes the regional lung deposition of the radioactive aerosols by combining the International Commission on Radiological Protection (ICRP) calculation model with the measured aerodynamic diameter distributions. The combination of the lung deposition calculation and the high-resolution detection in 500 size classes improved the existing methods by measuring the aerodynamic diameter distributions of the aerosol particles generated during the plasma arc cutting of various metals, such as steel alloys (304 and 316 stainless steel alloys, and mild steel), aluminum, copper, and brass. The sampling and characterization of aerosols in the size range of 6 nm–10 µm were performed using a high-resolution electrical low-pressure impactor (HR-ELPI⁺). We also investigated the distributions of aerosols, relative ratios of PM_{2.5}, PM_{0.1}, and PM_{0.01}, and the effect of alloying components on the aerodynamic diameter distribution. The measured data aided the calculation of the deposition ratios in different lung regions. Further, we analyzed the uncertainties of the lung deposition calculations using the low-resolution aerodynamic diameter data. Moreover, the study analyzed the limitations due to the lack of data in particle sizes smaller than 6 nm and the adoption of non-radioactive simulated specimens.

2. Materials and methods

2.1. Aerosol chamber and metal cutting conditions

We designed a 130-cm wide, 100-cm long, and 66-cm high isolated aerosol chamber to measure the generated aerosol particles without external leakage. A high-efficiency particulate air filter system installed on the left side of the chamber facilitated a continuous supply of clean air. The automatic cutting system designed for the reproducibility of the experiments comprises a dross box, servo-motor, programmable logic controller, and touchscreen. A plasma cutter (Powermax125, Hypertherm) was fixed at the center of the chamber ceiling. The movable table controlled by the servo-motor system on X-axis helped the metal plate cut automatically at a constant speed of 1 cm/s. In all experiments, the plasma arc torch current was set to 75 A and cutting lengths of 3 cm. The plasma cutting on steel alloys (SS304, SS316L, and mild steel) and aluminum plates produced a kerf of around 0.3 cm. When cutting copper and brass samples, the smallest value of kerf that can be obtained was 0.27 cm. The generated aerosol was measured for 4 min after completing the cutting process. During this period, the aerosol concentration reduced to the background level.

2.2. Physical and chemical properties of the sample metal plate

In the nuclear industry, the change in the chemical composition of materials by irradiation is negligible, except in the case of nuclear fuel. Table 1 presents the calculated results considering the transmuted ratio of the inner components of a reactor pressure vessel maintained at an extremely high neutron flux [51]. Despite the high value of neutron flux, the ratio of the maximum transmuted mass to the total mass is 0.2 w/w%. Therefore, the chemical composition of the activated materials is similar to that of the non-activated materials.

Six different 10-mm thick metal samples with varying chemical compositions that obtained an inspection certificate sheet from a certification company were selected for plasma cutting (Table 2) and placed on the dross box. According to the inspection certificate, the aluminum used in the experiment contained approximately 0.6% silicon and 1% magnesium; it was identified as an alloy of AA6061 in accordance with the Atomic Absorption Spectroscopy standard [52].

Copper alloys were identified using the unified numbering system (UNS), wherein families of alloys are categorized considering their elemental composition. According to the UNS standard, the copper samples were equivalent to C11000, with a minimum purity of 99%. Brass is an alloy of copper and zinc. The brass samples used in our experiment were categorized as C26000 with approximately 39% zinc content [53].

Two types of stainless steel and one low carbon steel (mild steel) were used in the experiment. Stainless steel comprises varying contents of chromium and nickel depending on the type of steel. Furthermore, adding molybdenum, copper, silicon, aluminum, titanium, and niobium renders the stainless steel with specific properties, such as halogen fitting and oxidation resistance. The SS316L type used in the experiment contained approximately 2% manganese and more nickel compared to the SS304 type. Conversely, low carbon steel must not exceed the maximum content specified for manganese (1.65%), silicon (0.60%), and copper (0.60%). We confirmed that the SS304, SS316L, and mild steel used in the experiments satisfied the inspection certificate sheet as per S30400, S31603, and G10180 UNS standards, respectively [54].

2.3. Properties of the aerosol measurement system

Metal cutting using a plasma arc cutter generated aerosols at the chamber center. These aerosols were released externally through sampling pipes (7.03 cm diameter) connected to the side of the aerosol chamber. A certain number of released aerosols were analyzed using an isokinetic sampler. The sampling point was positioned at the center of the sampling pipe. As indicated in Fig. 1, the length between the sampling point and the entrance of the sampling pipe was 60.4 cm. The aerosol measurement was performed using HR-ELPI⁺ (DEKATI). The number of aerosols generated exceeded the HR-ELPI⁺ measurement limit. Therefore, a diluter (eDiluter, DEKATI) with a fixed dilution factor of 1:64 was

Table 1

Transmuted ratio of nuclides in the components of the reactor pressure vessel after completing the reactor operation. Results were drawn using the data reported by Robertson et al. [51].

Components	PWR Internals 304L Stainless Steel	BWR Internals 304L Stainless Steel
Shroud	0.2	0.073
Core Barrel	0.032	—
Thermal Pads	0.005	—
Vessel Cladding	0.0007	0.000005

Table 2

Inspection certificate of steel alloys (SS304, SS316L, and mild steel), aluminum, copper, and brass, including the size specification of the metal plate, chemical composition, and melting point.

Metal Type	Aluminum ^a	Copper ^b	Brass ^b	SS304 ^c	SS316L ^c	Mild Steel ^c
Plate size [mm]	Thickness Width Length			10.0± 0.3 1600± 3.0 5000± 3.0		
Chemical composition [wt%]	Al:97.4, Mg:0.9, Si:0.59, Fe:0.40, Cu:0.28	Cu: 99.9	Cu:64.3, Zn:35.7, Fe:0.009, Pb:0.009	Cr:17.5–19, Ni: 8–12, Mn:2, N:0.1, Si:0.75, P:0.045, S:0.03, C:0.03	Cr:16–18, Ni:10–14, Mo:2–3, Mn:2–3, N:0.1, Si:0.75, P:0.045, S:0.03, C:0.03	Mn:0.6–0.9, C:0.2, S:0.05, P:0.04
Melting point [°C]	660	1085	900–940	1400–1455	1390–1440	1350–1530

^a Aluminum alloys is categorized as AA 6061 which have Mg and Si are the principal alloying elements.

^b Copper and Brass are categorized as UNS C11000 and C26000.

^c SS304, SS316L, and Mild Steel are categorized as UNS S30400, S31603, and G10180.

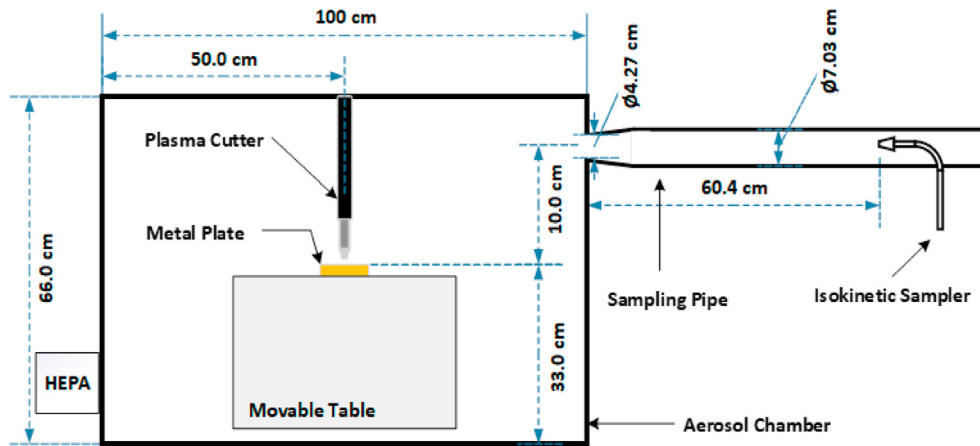


Fig. 1. Schematic of the metal cutting system and aerosol collection system. Aerosols generated during metal cutting were captured by the isokinetic sampler using the air-flow generated in the exhaust system.

connected before the HR-ELPI⁺ input port.

HR-ELPI⁺ is an advanced version of the electric low-pressure impactor (ELPI⁺, DEKATI), which provides number distribution at high resolution using an advanced iterative inversion calculation method. Unlike a typical cascade impactor with less than 20 inertial-based classes, HR-ELPI⁺ calculates the number distributions of aerosols with 500 size classes. In addition, HR-ELPI⁺ can be used also in standard ELPI⁺ mode by changing the detection settings. HR-ELPI⁺ comprises a unipolar corona charger, cascade impactor, and sensitive electrometers. The particles charged by the unipolar corona charger transmit electrical signals to 14 collection stages. The measured current signals are converted into the number concentrations using the particle-size-dependent relationships that determine the properties of the charger and impactor stages. Particles with sizes ranging from 6 nm to 10 μm are collected in each of the different-sized 14 stages. Owing to the broad range of measurement (6 nm–10 μm), linear scales deem the distinction of the peaks in the distribution data difficult. Therefore, the size distribution function is plotted in a lognormal form. The particle number per logarithmic diameter, denoted by “dN/dlogDp,” is plotted along the Y-axis, wherein dN and dlogDp represent the number of particles in the range and the log difference of the aerodynamic diameter widths, respectively. The subtraction of the log of the upper stage (logDp,u) and that the lower stage (logDp,l) aerodynamic diameters determine the dlogDp in HR-ELPI⁺ properties. The 50% cut-off diameters of the collection stages were 0.006, 0.0146, 0.0289, 0.0541, 0.0946, 0.155, 0.256, 0.381, 0.602, 0.947, 1.63, 2.47, 3.65, 5.36, and 9.88 μm.

2.4. Performance and calculation method of ELPI⁺ and HR-ELPI⁺

ELPI⁺ measures the aerodynamic diameter distributions of the aerosol particles in the range of 6 nm–10 μm. ELPI⁺ measured the raw current when charged particles are attached on each stage. Therefore, the electric currents measured by the ELPI⁺ electrometers rely on the charger performance. The measured current value was converted into the aerosol concentrations using the software. Equations (1)–(3) explain the relationship between the charging efficiency and particle-size distributions.

$$X(d_i) = 1.83d_i^{1.225} \quad (d_i < 1.035 \mu\text{m}), \quad (1)$$

$$X(d_i) = 1.8114d_i^{1.515} \quad (1.035 \mu\text{m} < d_i < 4.282 \mu\text{m}), \quad (2)$$

$$X(d_i) = 3.3868d_i^{1.085} \quad (4.282 \mu\text{m} < d_i), \quad (3)$$

where d_i is the geometric mean of a channel (aerodynamic diameter), and X is the charging efficiency.

After determining the charging efficiency, the number and mass concentrations are calculated using equations (4) and (5).

$$dN[1/\text{cm}^3] = \frac{C_i \times \text{Dilution}}{X(d_i)}, \quad (4)$$

$$dM \left[\text{mg} / \text{m}^3 \right] = \frac{C_i \times \left(\frac{\pi d_i^3}{6} \right) \times \text{Dilution} \times \text{Density} \times 0.001}{X(d_i)}, \quad (5)$$

where C_i is the measured current value.

Generally, the measurement accuracy relies on the particle size, as the charge effect of a large particle is significantly higher than that of a small particle. Therefore, the measurement sensitivity of the number concentration is better with large particles, whereas in the case of mass concentration, a contradictory behavior is observed; a small error in the data causes a large mass value change when considering large particles.

HR-ELPI⁺ has the same principle of measurement as ELPI⁺, but a calculation method has been applied to obtain a high resolution aerosol size distribution. The inversion calculation method is based on the kernel functions and iterative calculations. Although the calculation method for evaluating the mass size distribution still require additional research, the iterative inversion calculation method improves particle size resolution, allowing 500 data to be identified using 14 existing data in number size distribution. However, a previous study confirmed that the performance of HR-ELPI⁺ limits at a certain size range [55]. Although the HR-ELPI⁺ inversion worked efficiently at low levels of electrical noise, more than 1% of electrical noise levels caused a significant error in the size distribution. A large electrical error of 2–10% was observed in the small particle-size range of approximately 10 nm. However, if the electrical noise of ELPI⁺ is 0.1–1 fA, and the raw electric current exceeds 100 fA in actual measurement, the error is expected to decrease to less than 1%. Regardless, both HR-ELPI⁺ and ELPI⁺ encounter difficulties in measuring the concentrations of particles sized less than 10 nm because the lowest impactor cut-off is 16 nm and that of the filter stage is 6 nm.

2.5. Regional lung deposition model

The fundamental mechanism of aerosol inhalation and deposition are described in the ICRP publications. Most risk assessments of aerosols are used as biokinetic models listed in ICRP 68 [56] in the human respiratory tract model (ICRP 66) [57] and gastrointestinal tract model (ICRP 30) [58]. However, the mathematical model considered each region of the respiratory tract, such as the extrathoracic, bronchial, and alveolar-interstitial regions, as an equivalent particle filter acting in series. Equation (6) calculated the filtering efficiency of each compartment.

$$\eta_i = 1 - e^{-aR^p}, \quad (6)$$

where η_i is the filter efficiency of the i th compartment, and e , a , and R^p are the constant values obtained from the ICRP experimental data.

A volume of tidal flow that reaches each region and filtration efficiency of each region is considered to calculate the efficiencies of preceding filters in the series. Deposition ratios of aerosols are calculated using semi-empirical equations obtained by substituting the experimental data as functions of the particle size and flow. The deposition in each region of the respiratory tract is calculated as the ratio of aerosol deposited in the compartment using equation (7) [59,60].

$$D_i = D_{i-1} \eta_i \varepsilon_i \left(\frac{1}{\eta_{i-1}} - 1 \right), \quad (7)$$

where D_i and ε_i represent the deposition ratio and volume of i th compartment, respectively.

The aerosol size determines the fractional deposition of aerosol

in the nasopharyngeal, tracheobronchial, and alveolar regions. Impaction, diffusion, and interception are the three mechanisms that determine the deposition in different regions of the respiratory tract [61,62]. Particles larger than 1 μm deposit primarily in the upper airways following the dominant impaction mechanism, whereas particles smaller than 1 μm reach the deep parts of the lungs, depositing in the tracheobronchial and alveolar regions, following the diffusion mechanism.

3. Results and discussions

3.1. Number distribution of aerosols generated during plasma cutting of steel alloys

The number distributions of aerosols considering the aerodynamic diameters were measured and compared for various steel alloys, such as SS304, SS316L, and mild steel. The obtained results were quantitatively analyzed by calculating the fine particle fraction (FPF) to confirm the effect of the chemical composition of steel on the PM generation. The FPFs were categorized into three groups, i.e., $\text{PM}_{0.01}$, $\text{PM}_{0.1}$, and $\text{PM}_{2.5}$, based on the aerodynamic diameters of the aerosol of less than 0.01, 0.1, and 2.5 μm , respectively.

As depicted in Fig. 2(a) and (b), the number aerodynamic diameter distributions of aerosols generated during the plasma arc cutting of the steel alloys (SS304, SS316L, and mild steel) exhibited a similar trimodal distribution with three peaks at 0.01, 0.15–0.2, and 4–9 μm . The steel alloys were cut under controlled conditions, such as the cutting speed, material thickness, and current. An automatic cutting system, described in Section 2.1., was employed to enhance the reproducibility of the cutting process.

Peak patterns are governed by the mechanism of aerosol generation and development; aerosol develops from small nuclei to particles with large diameters. Nuclei generate during the metal cutting process under extreme conditions and develop using condensation, coagulation, and agglomeration processes, including particle collision [63–65]. The trimodal aerodynamic diameter distribution indicates that the dominant mechanism of aerosol generation during plasma arc cutting is vaporization [18,66,67]. The evaporation leads to a peak in the case of 0.1 μm size. However, after the generation of aerosol seeds, particles larger than 1 μm are formed during the nuclei development to create a peak in 4–9 μm range [6].

Most of the aerosols generated were identified as $\text{PM}_{2.5}$. The total number concentrations for SS304, SS316L, and mild steel were 5,801,809, 5,271,693, and 11,502,909 particles/ cm^3 , respectively. Table 3 indicates that higher concentrations of $\text{PM}_{0.01}$, $\text{PM}_{0.1}$, and $\text{PM}_{2.5}$ were present in mild steel cuts than in the cuts of other steel alloys. As depicted in Fig. 2(c), $\text{PM}_{0.1}$ and $\text{PM}_{0.01}$ increased during the cutting of mild steel compared to other steel alloys. The aerosol concentration during the cutting of mild steel was more than twice that generated during the SS304 and SS316L cutting. In addition, the ratio of $\text{PM}_{0.1}$ was 41.8% for mild steel cuts, whereas those of SS304 and SS316L were 17.9% and 26.9%, respectively. Table 3 shows that the ratio of $\text{PM}_{0.01}$ generated from mild steel was 5.99%, which is twice and 140 times higher than that of SS316L (2.41%) and SS304 (0.0429%), respectively. The different fractions of $\text{PM}_{0.01}$, $\text{PM}_{0.1}$, and $\text{PM}_{2.5}$ were caused by the different elemental compositions of alloys. Oki et al. proved that the different component proportions of metal alloys affect the aerodynamic diameter distribution [18] and Chae et al. confirmed that the vapor pressures of chemical elements are proportional to the micro-particle fraction of the aerosol [6].

Several shoulder-like peaks are observed in the size range of approximately 0.01–1 μm (Fig. 2(a)). This is because the aerosols interact with other particles during their development, wherein their shapes and physicochemical properties vary. The interactions

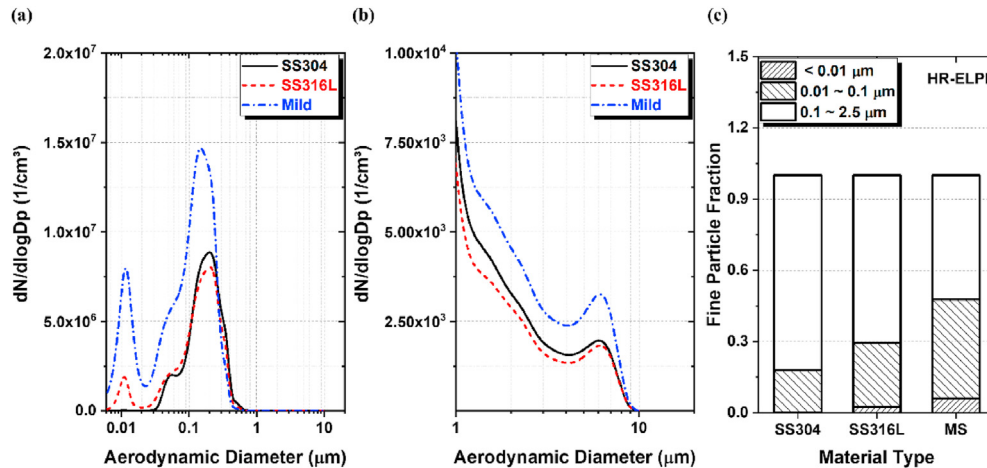


Fig. 2. (a) Number aerodynamic diameter distribution of three different steel alloys (SS304, SS316L, and mild steel) under operating conditions of 75 A plasma arc current and 3 cm cutting length. (b) A hidden peak in 1–10 μm from (a). (c) Comparison of the fine particle fractions (FPFs) defined using the number fraction of aerosols below the 0.01, 0.1, and 2.5 μm range.

Table 3

Number concentrations of steel alloys (SS304, SS316L, and mild steel) during plasma cutting with 3 cm cutting length. The concentration of the particulate matter in the aerodynamic diameter region is divided into three different ranges: under 0.01, 0.1, and 2.5 μm.

Material	CMAD ^a [μm]	Number concentration [# /cm ³]		
		PM _{0.01}	PM _{0.1}	PM _{2.5}
SS304	0.166	2180	910,304	5,081,809
SS316L	0.146	127,250	1,548,323	5,271,693
Mild Steel	0.102	689,429	5,497,493	11,502,909

^a CMAD is count median aerodynamic diameter, which means the half of the particle have an aerodynamic diameter smaller than that value.

induce several peaks in the larger diameter range of the aerosols. Moreover, these peaks were possibly induced owing to the contribution of different chemical compositions of the original samples to the distributions of aerosols. Additionally, the overlapped peaks can originate from different nuclei, with varying initial chemical compositions. For instance, mild steel contains less chromium and nickel compared to other steel alloys. By contrast, chromium and nickel are the primary ingredients of SS304 and SS316L, contributing approximately 30% to the total chemical composition.

3.2. Effect of alloying components on number distributions of aerosols

Section 3.1 described the relative difference of alloying elements in terms of vapor pressure and its effect on the different distributions of aerosol size. For a deeper understanding, additional experiments with aluminum, copper, and brass were conducted to compare the results with that of the plasma cutting of steel alloys. Although aluminum, copper, and brass are rarely used in commercial reactors in high-temperature environments, these materials are commonly used as structural components in accelerators [18,68]. Moreover, aluminum alloys are generally used as nuclear fuel claddings in research reactors [69].

As illustrated in Fig. 3(a) and (b), most aerosols generated during the plasma arc cutting of aluminum, copper, and brass are PM_{2.5}, similar to steel alloys. However, the number aerodynamic distribution of each metal is different. Aluminum presents a bimodal

distribution, wherein peaks of similar heights are identified at 0.01 and 0.04 μm. The highest and the second-highest peaks for copper are observed at 0.01 and 0.15 μm, respectively. These differences of size distributions can be explained by the vapor pressure and melting point of the element. The vapor pressure of copper at melting point (5.9×10^{-2} Pa) is much higher than that of aluminum (3.4×10^{-7} Pa). According to a previous study [6], the FPF increases with the vapor pressure of the element. Therefore, the average aerosols size of copper is less than that of aluminum. By contrast, a single peak exists at 0.3 μm in the case of brass, unlike the distributions of aluminum and copper (Fig. 3(a)). Although the primary ingredient in brass is copper, the distribution is different compared to that of the aerosols generated in copper samples owing to the differences in vapor pressures between copper and zinc. In addition, the boiling point of zinc (907 °C) is lower than the melting temperature of brass (940 °C). Hence, zinc can be boiling, which can induce the liquid droplet explosion generating larger-sized aerosols.

3.3. Comparison of aerosol distribution data between ELPI⁺ and HR-ELPI⁺

We compared the data collected using two different modes, HR-ELPI⁺ and ELPI⁺, to confirm the effect of size resolution on the measured number distributions.

The resolution of number distributions in the measurement system significantly affects the FPFs. A low-resolution measurement can lead to the overestimation of the aerosol concentration below 0.1 μm. Fig. 4 indicates that the values of PM_{0.1} measured for the three samples, aluminum, copper, and brass, using ELPI⁺ were higher than that of HR-ELPI⁺. PM_{0.1} of aluminum and brass in the ELPI⁺ mode are 1.5 and 3.5 times higher than that of the HR-ELPI⁺ mode, respectively. Contrastingly, the PM_{0.1} of copper reduces to 20% in ELPI⁺ measurements, and the difference in PM_{0.01} is higher than that of PM_{0.1}. When aerosols were measured using the low-resolution instrument (ELPI⁺), PM_{0.01} of aluminum, copper, and brass increased 8.5, 5, and 17 times, respectively, in comparison with the measurements using HR-ELPI⁺ (Table 4). However, the number concentration of aerosol can be incorrectly determined when using a low-resolution measurement system. Therefore, the aerosol properties measured using different instruments must be compared carefully.

The mechanism of aerosol generation can be interpreted

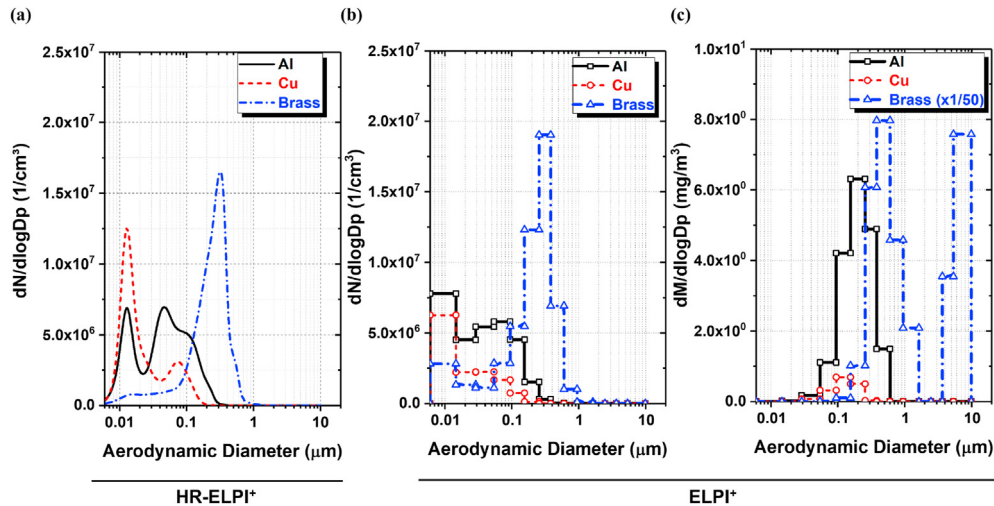


Fig. 3. (a) Number aerodynamic diameter distribution of aluminum, copper, and brass using HR-ELPI⁺. (b) Number and (c) mass aerodynamic diameter distributions of aluminum, copper, and brass using ELPI⁺. The cutting process operated at 75 A plasma arc current and 3 cm cutting length.

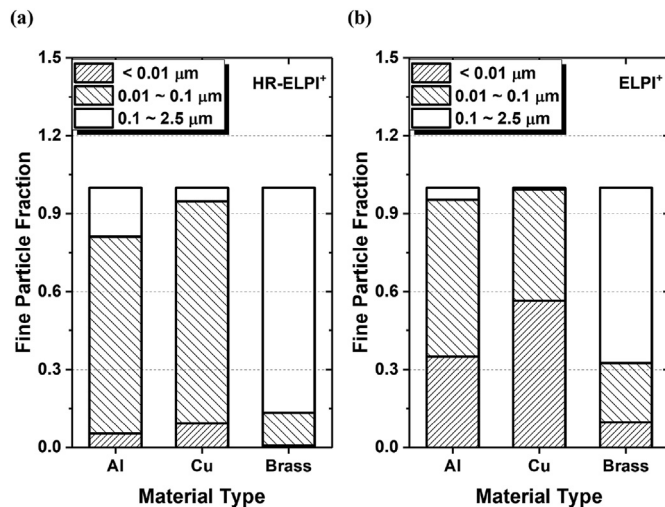


Fig. 4. Comparison of fine particle fractions (FPFs) defined by the number fractions of aerosols below the 0.01, 0.1, and 2.5 μm range for aluminum, copper, and brass using (a) high-resolution mode of ELPI⁺ (HR-ELPI⁺) and (b) ELPI⁺.

differently based on the measurement resolution. In low resolution, both the mass and number distributions were measured to obtain a single peak in the ranges of 0.0946–0.155 μm and 0.006–0.0146 μm in copper. By contrast, the number distribution of

aerosols from copper samples displayed two peaks in high-resolution measurement. In the case of brass, the peak at the smaller size range, approximately 0.01 μm , was estimated to be higher in the ELPI⁺ mode than the HR-ELPI⁺. Typically, in the low-resolution measurement, both mass and number distributions resulted in a bimodal distribution with two peaks. The peaks in the mass and number distributions were identified in the ranges of 0.381–0.602 μm and 5.36–9.88 μm , and 0.006–0.0146 μm and 0.256–0.381 μm , respectively (Fig. 3(b) and (c)). Moreover, the two peaks shifted their locations. For example, aluminum presented peaks at 0.01 and 0.04 μm in the high-resolution measurement, whereas these peaks were observed in the ranges 0.006–0.0146 μm and 0.0541–0.0946 μm in the low-resolution measurement.

3.4. Particle distribution based on the chemical composition of the material

Although non-radioactive materials simulated the radioactive aerosol generation, the experimental results can be applied to predict the generation of radioactive aerosols during the plasma arc cutting. The isotopes do not contribute to the aerodynamic diameter distribution of aerosols, as the radioactivity is governed by the mass distribution of aerosols [6]. Therefore, the measured mass distribution of non-radioactive aerosols is essentially identical to the mass distribution of radioactive aerosols, provided that the chemical composition (element composition) in the cutting materials is identical. The subsequent paragraphs validate that

Table 4

Number concentrations of aluminum, copper, and brass during plasma cutting with 3 cm cutting length. The concentration of particulate matter in the aerodynamic diameter region is divided into three different ranges: under 0.01, 0.1, and 2.5 μm .

Material	Measurement mode	CMAD ^a [μm]	MMAD ^b [μm]	Number concentration [#/cm ³]		
				PM _{0.01}	PM _{0.1}	PM _{2.5}
Aluminum	ELPI ⁺	0.029	0.190	3,009,046	8,203,356	8,593,349
	HR-ELPI ⁺	0.0433	N.A.	352,886	5,313,545	6,550,561
Copper	ELPI ⁺	0.018	0.117	2,418,428	4,250,831	4,277,466
	HR-ELPI ⁺	0.0155	N.A.	491,310	5,013,575	5,284,715
Brass	ELPI ⁺	0.152	1.32	1,087,585	3,653,059	11,218,803
	HR-ELPI ⁺	0.237	N.A.	63,294	1,042,456	7,776,101

^a CMAD is count median aerodynamic diameter, which means the half of the particle have an aerodynamic diameter smaller than that value.

^b MMAD is mass median aerodynamic diameter.

radioactivity is governed by the mass distribution, and the isotopes do not contribute to the aerodynamic diameter distribution. Additionally, the simulation of radioactive aerosols through non-radioactive materials using plasma arc cutting is explained.

Oki et al. measured the radioactivity and the mass of radioactive aerosols generated during the plasma arc cutting of activated stainless steel 304 and iron [18]. The radioactivities of ^{51}Cr , ^{59}Fe , and ^{65}Zn radionuclides were measured using a high-resolution Ge semiconductor detector; the masses of Cr and Fe elements were measured using inductively coupled plasma emission spectrometry. As indicated in Fig. 5(a), the activity median aerodynamic diameter (AMAD) of radioisotopes (^{51}Cr , ^{59}Fe , and ^{65}Zn) maintain a well-fitted linear relationship with the corresponding mass median aerodynamic diameter (MMAD) of elements (Cr, Fe, and Zn), wherein the obtained R-squared value is 0.7789. In addition, the FPFs in 0.1, 1, and 2.5 μm ranges present a better linear relationship between radionuclides (^{51}Cr , ^{59}Fe , and ^{65}Zn) than between the elements (Cr, Fe, and Zn) (Fig. 5(b)). Therefore, the radioactivity distribution can be estimated using the mass distribution based on the linear relationship, validating that it is governed by the mass distribution of aerosols generated during the plasma arc cutting.

Fig. 6 illustrates the calculated AMAD and FPF of the radioactive aerosols generated during the plasma arc cutting of activated metals (stainless steel 304 and brass). As indicated in the figure, the AMAD difference between the isotopes is negligible in comparison with the same materials used in the cutting process [18]. For cobalt isotopes (^{57}Co , ^{58}Co , and ^{60}Co from activated stainless steel 304), the maximum difference of AMAD is 0.05 μm , and the differences of AMAD of isotopes from stainless steel 304 (^{52}Mn and ^{54}Mn) and brass (^{57}Co and ^{58}Co) are less than or equal to 0.01 μm . Additionally, the FPFs of all the isotopes are nearly identical. Therefore, as the AMAD and FPF between isotopes were identical when the same materials were used in the cutting process, we concluded that the isotopes do not contribute to the aerodynamic diameter distribution.

Based on Figs. 5 and 6, we confirmed that the radioactivity distribution can be estimated using the mass distribution of aerosols by maintaining the chemical composition in non-activated materials identical to the activated materials. In addition, a

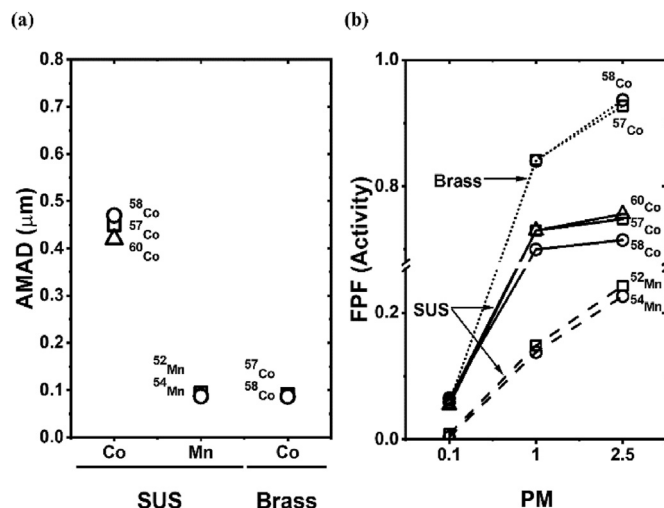


Fig. 6. (a) Activity median aerodynamic diameter (AMAD) of radioisotopes (^{57}Co , ^{58}Co , ^{60}Co , ^{52}Mn , and ^{54}Mn) present in the radioactive aerosols generated during the plasma arc cutting of stainless steel 304 and brass. (b) Fine particle fractions (FPF) of radioisotopes. All data were obtained from the study reported by Oki et al. [18].

maximum variation of 0.2 w/w % can occur during the irradiation under an extremely high neutron flux environment [51], as explained in Section 2.2. Therefore, non-activated materials can simulate the radioactive aerosols to calculate the radiation dose absorbed during inhalation.

3.5. Deposition of aerosol particles in the respiratory tract based on the aerodynamic size

To assess the biological risk of aerosols, detailed information on particle-size distribution is required, as the ratio of partial deposition on the lungs is determined primarily by the particle size of the aerosol. We identified the effect of the measurement equipment performance on the prediction of aerosol deposition in the respiratory tract by comparing the calculated deposition ratios of aerosols obtained from HR-ELPI⁺ and ELPI⁺ data. We also calculated the FPF to quantify the impact on the prediction of aerosol deposition.

Typically, both in vivo and in vitro studies determine the aerosol deposition in the human respiratory tract. However, a limitation exists in the experimental models when simulating realistic physiological conditions. Moreover, the lung deposition analysis based on clinical trials raises ethical issues despite being highly useful [70]. To overcome these limitations, several mathematical models of human respiratory systems have been developed to calculate the deposition ratio of inhaled aerosols [60,71–75]. The human respiratory tract model (HRTM) [57] is widely used to estimate the radiation dose resulting from exposure to radioactive aerosols. The aerodynamic size of aerosol significantly affects the ratio of deposition in the different regions of the respiratory tract, such as nasal, pharyngeal, laryngeal, trachea, bronchiole, and alveolar sacs [76]. The deposition in the top portion of the lung reduces as the particle size decreases to submicron dimensions. However, with the further decrease in particle size to a nanometer scale, the deposition in the top portion of the lung increases to levels that equal or remain higher than those of the micronized particles [77]. Conversely, the aerosols in the size range of 0.01–0.1 μm are chiefly deposited in the alveolar region (Fig. 7).

The risk of aerosol inhalation is based on the mass median aerodynamic distribution. However, the number distribution is vital when the size of particles is smaller than 0.1 μm [78]. Initially, mass distribution was considered a useful factor, connecting a wide

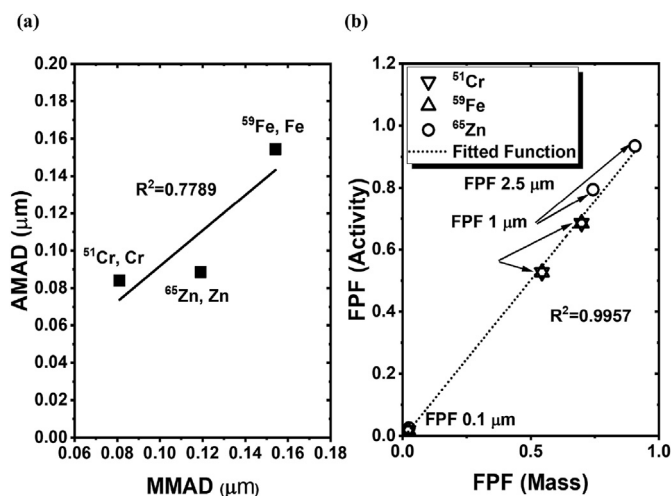


Fig. 5. (a) Linear relationship between activity median aerodynamic diameter (AMAD) and mass median aerodynamic diameter (MMAD) between the following isotopes and elements: ^{51}Cr vs Cr, ^{59}Fe vs Fe, ^{65}Zn vs Zn, obtained from the aerosols generated during the plasma arc cutting of activated stainless steel 304 (^{51}Cr , Cr), iron (^{59}Fe , Fe), and brass (^{65}Zn , Zn). (b) The fine particle fractions (FPF) of radioisotopes and elements. All data were obtained from the study reported by Oki et al. [18].

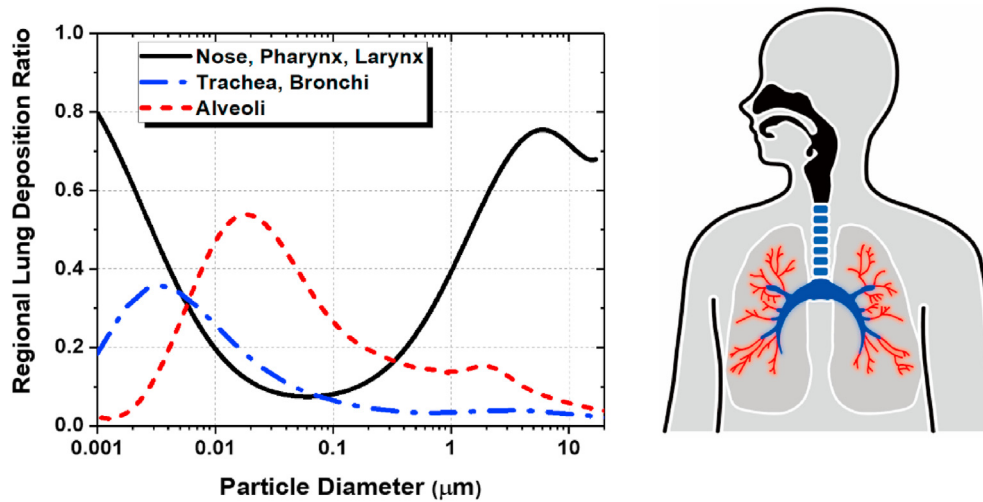


Fig. 7. Regional particle deposition in the lungs based on the particle diameter considering the ICRP human respiratory tract model [57]. Deposition of inhaled particles in the nasopharyngeal, tracheobronchial, and alveolar regions of the human respiratory tract, under the conditions of breathing through the nose at rest, was calculated using the ICRP mathematical model.

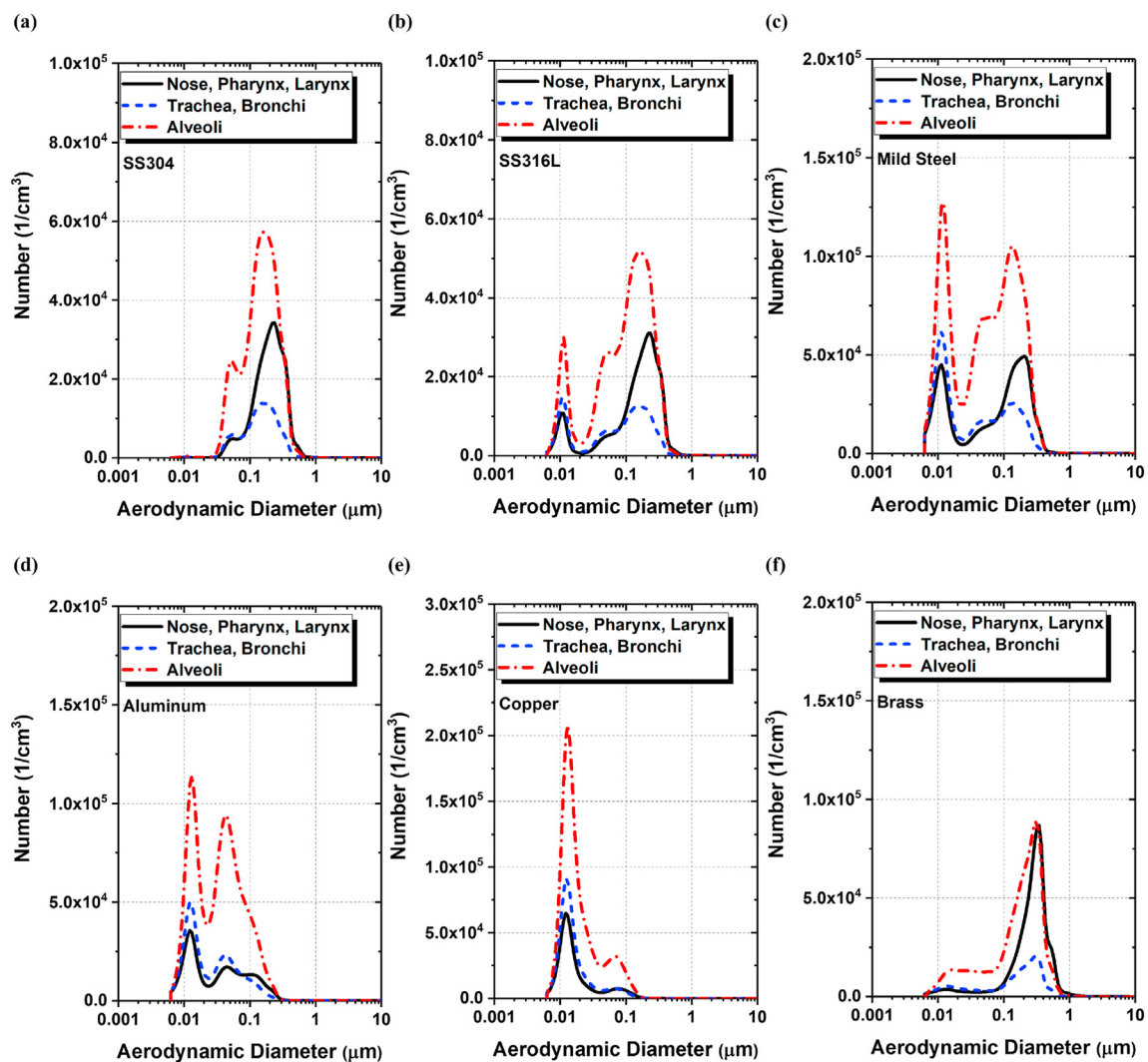


Fig. 8. Number distribution of aerosols deposited in three areas of the respiratory tract predicted by the ICRP model considering the aerodynamic diameter using HR-ELPI+ mode data. Six metal samples are compared, namely (a) SS304, (b) SS316L, (c) mild steel, (d) aluminum, (e) copper, and (f) brass.

range of aerosol distributions and health outcomes; however, multiple cases validated that mass is insufficient to assess risks, particularly in nanoscale aerosols [79–82]. Although the contribution of the mass fraction of nanoparticles to the total mass of aerosols is negligible, these particles can be significantly harmful. For instance, aerosol can increase the risk of cancer by reaching the alveolar region and moving toward other sensitive organs, such as the thyroid and brain, through the bloodstream. Therefore, several studies identified better symptoms to determine the biological toxic effects of aerosols, such as inflammatory and oxidative stress reactions, that rely on the number or shape of the particles rather than the mass [78,83,84].

To predict the number of aerosols deposited in each lung region, the partial deposition ratios were multiplied with the number of distribution data of HR-ELPI⁺ and ELPI⁺. Figs. 8 and 9 depict the number distributions of aerosols deposited in three areas of the respiratory tract using data from HR-ELPI⁺ and the low-resolution ELPI⁺ modes, respectively. The deposition ratios vary significantly depending on the type of metal. Furthermore, the deposition ratios in the alveolar sacs are dominant in regions of all sizes because the number concentration of aerosols generated during metal cutting was typically less than 1 μm .

Table 5

Regional particle deposition in three classified regions of the lungs depending on the resolution mode of ELPI⁺.

Material	Measurement mode	Total particles deposition in lung [%]			PM _{0.1} deposition in lung [%]		
		ET ^a	TH ^b	Alveoli	ET ^a	TH ^b	Alveoli
SS304	ELPI ⁺	10.4	8.7	30.4	10.1	12.7	40.5
	HR-ELPI ⁺	11.3	5.4	22.5	7.8	8.4	34.3
SS316L	ELPI ⁺	10.5	6.6	25.8	8.6	10.4	38.1
	HR-ELPI ⁺	11.4	7.1	25.6	10.5	12.7	38.8
Mild Steel	ELPI ⁺	10.8	9.5	31.0	10.9	13.8	31.9
	HR-ELPI ⁺	11.4	9.9	30.8	12.0	15.2	41.6
Aluminum	ELPI ⁺	13.1	16.1	40.8	12.1	15.9	39.0
	HR-ELPI ⁺	10.8	12.8	39.4	11.0	14.5	43.3
Copper	ELPI ⁺	15.7	20.3	44.4	15.4	20.2	43.7
	HR-ELPI ⁺	13.3	17.8	46.1	13.5	18.5	47.3
Brass	ELPI ⁺	14.8	7.3	23.7	9.5	12.2	29.2
	HR-ELPI ⁺	14.1	5.5	21.4	10.4	13.3	41.6

^a ET is an acronym for the extrathoracic region, including the nasal and oral passages, pharynx, and larynx.

^b TH is an acronym for the thoracic region, including the trachea and bronchiole region.

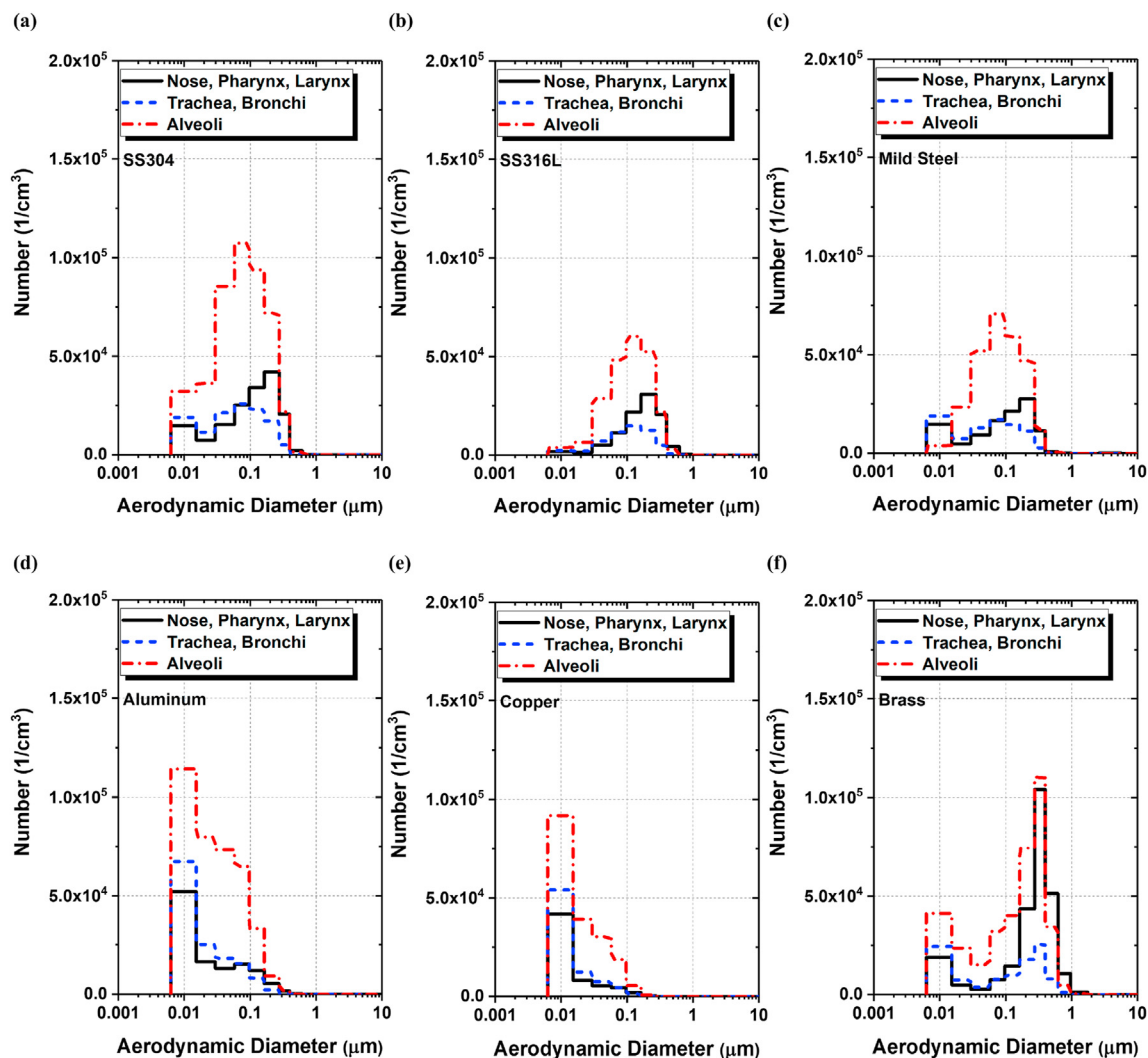


Fig. 9. Number distribution of aerosols deposited in three areas of the respiratory tract predicted by the ICRP model considering the aerodynamic diameter using ELPI⁺ mode data. Six metal samples are compared, namely (a) SS304, (b) SS316L, (c) mild steel, (d) aluminum, (e) copper, and (f) brass.

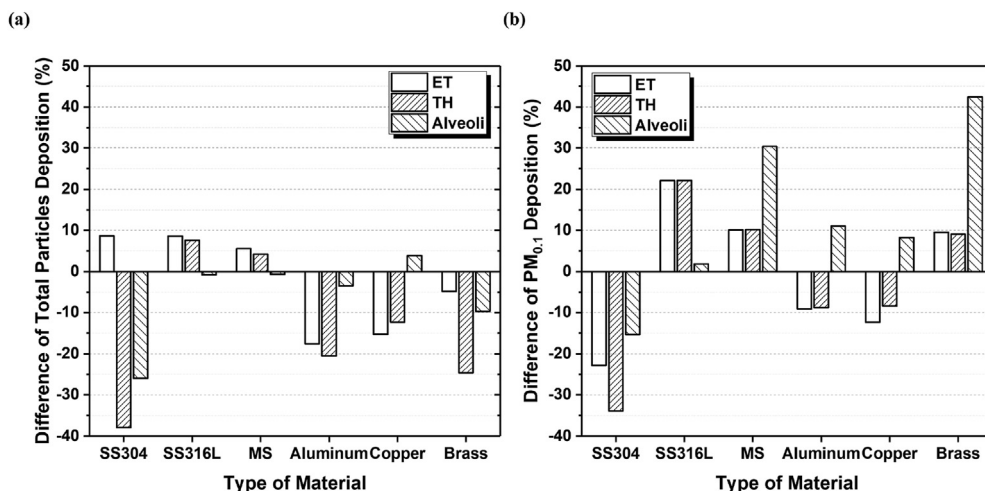


Fig. 10. Difference ratio depending on the resolution mode of ELPI⁺ for (a) total particle deposition and (b) PM_{0.1} deposition in three areas of the respiratory tract. ET represents the extrathoracic region, including the nasal and oral passages, pharynx, and larynx. TH represents the thoracic region, including the trachea and bronchiole region.

As presented in Table 5, the alveolar depositions obtained from the HR-ELPI⁺ data were higher than that of ELPI⁺ in all cases, except for the aerosols generated during the SS304 cutting. This is because the predicted alveolar deposition of aerosols is maximum in the range of 0.01–0.1 μm. Fig. 4 confirms that the FPF of aerosols in the range of 0.01–0.1 μm calculated using the HR-ELPI⁺ data is higher than that of ELPI⁺ data. Moreover, Fig. 10 validates the effect of the change in the measurement mode (HR-ELPI⁺ versus ELPI⁺) on the prediction of the deposited aerosols as a percentage change. Equation (8) calculates the differences in the partial deposition.

$$\Delta DR[\%] = \left(\frac{DR_{HR-ELPI}}{DR_{ELPI}} - 1 \right) \times 100, \quad (8)$$

where ΔDR is the difference in the deposition ratio, DR_{HR-ELPI} and DR_{ELPI} are the deposition ratios calculated using HR-ELPI⁺ and ELPI⁺ data, respectively.

In the alveolar deposition of PM_{0.1} generated during brass cutting, the deposition ratio difference between HR-ELPI⁺ and ELPI⁺ increased to a maximum of 42%. The percentage changes fluctuated significantly depending on the type of material and the partial region wherein the aerosols were deposited. However, PM_{0.1} deposition calculated using HR-ELPI⁺ was larger than that of ELPI⁺ in most metal alloys, excluding SS304. Consequently, PM_{0.1} was measured precisely in the high-resolution mode of ELPI⁺; the result was close to the predicted alveolar deposition ratio. Therefore, to assess the biological risk of PM, the number distribution of the nano-sized aerosols must be analyzed precisely. Thus, this study demonstrated the need for enhanced measuring equipment in the high-resolution mode by comparing the ELPI⁺ and HR-ELPI⁺ data.

Furthermore, the radioactivity distribution data must be analyzed to calculate the internal radiation doses. However, it is difficult to obtain actual radioactive metal samples from a nuclear power plant and establish a laboratory environment that follows radiation safety, unless the laboratory-scale study is government-approved. Therefore, an analytical method is required to obtain the aerodynamic distribution data of metal aerosols to compute the internal radiation doses. Additionally, the particle data in the size range of 1 nm–0.01 μm is essential because the alveolar region is a major deposition site wherein the particles are more inclined to penetrate the blood, reaching a maximum at approximately 50% deposition for nanoparticles under 0.01 μm. However, particles smaller than 6 nm cannot be measured owing to the measurement

limit of ELPI⁺. Additionally, the measurement error in the 10 nm size range significantly affects the calculation of particle deposition in the lungs. As the existing equipment cannot measure the aerosols in the range of 1 nm–10 μm [85–88], the performance of the equipment must be improved through further research.

4. Conclusions

To understand the effects of radioactive aerosols generated during the dismantling of nuclear facilities, this study focused on characterizing the aerosol contaminants using high-resolution measurements. Typically, the characteristics of aerosols generated during the plasma cutting are highly associated with the metal type used in the cutting process. We confirmed that the chemical composition of the cutting material significantly affects the aerodynamic diameter distribution and the number of aerosols generated. Moreover, the resolution of the aerosol instrument, used to calculate the lung deposition ratio of the aerosol, affects the measured number concentration of the nano-sized particles. The biological effect of the aerosols in the size range of 0.01–0.1 μm is significant, as the alveolar deposition is predominant. Therefore, a more accurate risk assessment is necessary to analyze the concentration of aerosol that can be safely inhaled, which requires further research into high-resolution measuring equipment.

Declaration of competing interest

The authors declare that they have no known competing financial interests or personal relationships that could have appeared to influence the work reported in this paper.

Acknowledgments

This work was supported by the National Research Foundation of Korea grant funded by the Ministry of Science and ICT, Korea (Grant No. NRF-2017M2A8A4018596) and the Korea Institute of Energy Technology Evaluation and Planning grant funded by the Ministry of Trade, Industry and Energy, Korea (Grant No. 20201520300060).

References

- [1] J. Onodera, H. Yabuta, T. Nishizoro, C. Nakamura, Y. Ikezawa, Characterization

- of aerosols from dismantling work of experimental nuclear power reactor decommissioning, *J. Aerosol Sci.* 22 (1991) S747–S750.
- [2] F.G. Cesari, M. Rogante, A. Giostri, Results of the experimental campaign on contaminated metal components parameters and suggestions for safely NPP component dismantling, *Nucl. Eng. Des.* 238 (2008) 2801–2810.
 - [3] S. Choi, W.I. Ko, Dynamic assessments on high-level waste and low- and intermediate-level waste generation from open and closed nuclear fuel cycles in Republic of Korea, *J. Nucl. Sci. Technol.* 51 (2014) 1141–1153.
 - [4] S. Choi, H.J. Lee, W.I. Ko, Dynamic analysis of once-through and closed fuel cycle economics using Monte Carlo simulation, *Nucl. Eng. Des.* 277 (2014) 234–247.
 - [5] C. Kim, S. Choi, M. Shin, Review—electro-kinetic decontamination of radioactive concrete waste from nuclear power plants, *J. Electrochem. Soc.* 165 (2018) E330–E344.
 - [6] N. Chae, M.H. Lee, S. Choi, B.G. Park, J.S. Song, Aerodynamic diameter and radioactivity distributions of radioactive aerosols from activated metals cutting for nuclear power plant decommissioning, *J. Hazard Mater.* 369 (2019) 727–745.
 - [7] M.-H. Lee, W. Yang, N. Chae, S. Choi, Performance Assessment of HEPA Filter against Radioactive Aerosols from Metal Cutting during Nuclear Decommissioning, *Nuclear Engineering and Technology*, 2019.
 - [8] M.-H. Lee, W. Yang, N. Chae, S. Choi, Aerodynamic diameter distribution of aerosols from plasma arc cutting for steels at different cutting power levels, *J. Radioanal. Nucl. Chem.* 323 (2020) 613–624.
 - [9] C. IAEA, Radioactive Particles in the Environment: Sources, Particle Characteristics, and Analytical Techniques, IAEA-TECDOC Vienna, 2011, p. 32.
 - [10] J. Severa, J. Bár, Handbook of Radioactive Contamination and Decontamination, Elsevier, 1991.
 - [11] K. Talaat, J. Xi, P. Baldez, A. Hecht, Radiation dosimetry of inhaled radioactive aerosols: CFPD and MCNP transport simulations of radionuclides in the lung, *Sci. Rep.* 9 (2019) 17450.
 - [12] J.K. Jakobsson, J. Hedlund, J. Kumlin, P. Wollmer, J. Londahl, A new method for measuring lung deposition efficiency of airborne nanoparticles in a single breath, *Sci. Rep.* 6 (2016) 36147.
 - [13] R. Fishler, P. Hofemeier, Y. Etzion, Y. Dubowski, J. Sznitman, Particle dynamics and deposition in true-scale pulmonary acinar models, *Sci. Rep.* 5 (2015) 14071.
 - [14] P. Demokritou, S.J. Lee, S.T. Ferguson, P. Koutrakis, A compact multistage (cascade) impactor for the characterization of atmospheric aerosols, *J. Aerosol Sci.* 35 (2004) 281–299.
 - [15] A. Jarvinen, M. Aitoma, A. Rostedt, J. Keskinen, J. Yli-Ojanpera, Calibration of the new electrical low pressure impactor (ELPI plus), *J. Aerosol Sci.* 69 (2014) 150–159.
 - [16] J. Keskinen, K. Pietarinen, M. Lehtimäki, Electrical low-pressure impactor, *J. Aerosol Sci.* 23 (1992) 353–360.
 - [17] M. Marjamäki, J. Keskinen, D.R. Chen, D.Y.H. Pui, Performance evaluation of the electrical low-pressure impactor (ELPI), *J. Aerosol Sci.* 31 (2000) 249–261.
 - [18] Y. Oki, M. Numajiri, T. Suzuki, Y. Kanda, T. Miura, K. Iijima, K. Kondo, Particle-size and fuming rate of radioactive aerosols generated during the heat cutting of activated metals, *Appl. Radiat. Isot.* 45 (1994) 553–562.
 - [19] J. Bernard, G. Pilot, J. Grandjean, Evaluation of Various Cutting Techniques Suitable for the Dismantling of Nuclear Components, EUR, Luxembourg), 1998.
 - [20] V.J. Novick, C.-J. Brodrick, S. Crawford, J. Nasiatka, K. Pierucci, V. Reyes, J. Sambrook, S. Wrobel, J. Yeary, Aerosol measurements from plasma torch cuts on stainless steel, carbon steel, and aluminum, in: Argonne National Lab, 1996.
 - [21] M. Ebadian, S. Dua, H. Guha, Size distribution and rate of production of airborne particulate matter generated during metal cutting, in: National Energy Technology Lab., Pittsburgh, PA (US), 2001.
 - [22] F. Schulze, X.H. Gao, D. Virzonis, S. Damiati, M.R. Schneider, R. Kodzius, Air quality effects on human health and approaches for its assessment through microfluidic chips, *Genes* 8 (2017) 244.
 - [23] P.E. Morrow, Possible mechanisms to explain dust overloading of the lungs, *Fund. Appl. Toxicol.* 10 (1988) 369–384.
 - [24] C.A. Pope III, R.T. Burnett, M.J. Thun, E.E. Calle, D. Krewski, K. Ito, G.D. Thurston, Lung cancer, cardiopulmonary mortality, and long-term exposure to fine particulate air pollution, *Jama* 287 (2002) 1132–1141.
 - [25] T. Zhang, B. Gao, Z. Zhou, Y. Chang, The movement and deposition of PM2.5 in the upper respiratory tract for the patients with heart failure: an elementary CFD study, *Biomed. Eng. Online* 15 (2016) 138.
 - [26] I.J. Yu, K.J. Kim, H.K. Chang, K.S. Song, K.T. Han, J.H. Han, S.H. Maeng, Y.H. Chung, S.H. Park, K.H. Chung, Pattern of deposition of stainless steel welding fume particles inhaled into the respiratory systems of Sprague–Dawley rats exposed to a novel welding fume generating system, *Toxicol. Lett.* 116 (2000) 103–111.
 - [27] P. Biswas, C.Y. Wu, Nanoparticles and the environment, *J. Air Waste Manag. Assoc.* 55 (2005) 708–746.
 - [28] J. Wang, T. Hoang, E.L. Floyd, J.L. Regens, Characterization of particulate fume and oxides emission from stainless steel plasma cutting, *Ann Work Expo Health* 61 (2017) 311–320.
 - [29] S. Ramakrishnan, M.W. Rogozinski, Properties of electric arc plasma for metal cutting, *J. Phys. D Appl. Phys.* 30 (1997) 636–644.
 - [30] D. Krajcarz, Comparison metal water jet cutting with laser and plasma cutting, 24th Daaam International Symposium on Intelligent Manufacturing and Automation 2013 (69) (2014) 838–843.
 - [31] T. Shimada, T. Tanaka, Characterization on the radioactive aerosols dispersed during plasma arc cutting of radioactive metal piping, *J. Radioanal. Nucl. Chem.* 303 (2015) 1345–1349.
 - [32] K.Y. Kirichenko, A.I. Agoshkov, V.A. Drozd, A.V. Gridasov, A.S. Kholodov, S.P. Kobyljakov, D.Y. Kosyanov, A.M. Zakharenko, A.A. Karabtsov, S.R. Shimanskii, A.K. Stratidakis, Y.O. Mezhuiev, A.M. Tsatsakis, K.S. Golokhvast, Characterization of fume particles generated during arc welding with various covered electrodes, *Sci. Rep.* 8 (2018) 17169.
 - [33] M. Oprya, S. Kiro, A. Worobiec, B. Horemans, L. Darchuk, V. Novakovic, A. Ennan, R. Van Grieken, Size distribution and chemical properties of welding fumes of inhalable particles, *J. Aerosol Sci.* 45 (2012) 50–57.
 - [34] P. Hewitt, Estimation of regional pulmonary deposition and exposure for fumes from SMAW and GMAW mild and stainless steel consumables, *Am. Ind. Hyg. Assoc. J.* 56 (1995) 136–142.
 - [35] M.P. Holsapple, W.H. Farland, T.D. Landry, N.A. Monteiro-Riviere, J.M. Carter, N.J. Walker, K.V. Thomas, Research strategies for safety evaluation of nanomaterials, part II: toxicological and safety evaluation of nanomaterials, current challenges and data needs, *Toxicol. Sci.* 88 (2005) 12–17.
 - [36] V. Voitkevich, Methods for studying welding fumes the Paton, *Weld. J.* 3 (1982) 51–54.
 - [37] N.T. Jenkins, W.M.G. Pierce, T.W. Eagar, Particle size distribution of gas metal and flux cored arc welding fumes, *Weld. J.* 84 (2005) 156s–163s.
 - [38] J.W. Sowards, J.C. Lippold, D.W. Dickinson, A.J. Ramirez, Characterization of welding fume from SMAW electrodes - Part I, *Weld. J.* 87 (2008) 106s–112s.
 - [39] J.W. Sowards, A.J. Ramirez, D.W. Dickinson, J.C. Lippold, Characterization of welding fume from SMAW electrodes - Part II, *Weld. J.* 89 (2010) 82s–90s.
 - [40] A.T. Zimmer, P. Biswas, Characterization of the aerosols resulting from arc welding processes, *J. Aerosol Sci.* 32 (2001) 993–1008.
 - [41] P.J. Hewitt, M.G. Madden, Welding process parameters and hexavalent chromium in mig fume, *Ann. Occup. Hyg.* 30 (1986) 427–434.
 - [42] J.F. Vanderwal, Further-studies on the exposure of welders to fumes, chromium, nickel and gases in Dutch industries - plasma welding and cutting of stainless-steel, *Ann. Occup. Hyg.* 30 (1986) 153–161.
 - [43] C.S. Yoon, N.W. Paik, J.H. Kim, Fume generation and content of total chromium and hexavalent chromium in flux-cored arc welding, *Ann. Occup. Hyg.* 47 (2003) 671–680.
 - [44] P. Stacey, O. Butler, Performance of laboratories analysing welding fume on filter samples: results from the WASP proficiency testing scheme, *Ann. Occup. Hyg.* 52 (2008) 287–295.
 - [45] B. Berlinger, M. Naray, I. Sajo, G. Zaray, Critical evaluation of sequential leaching procedures for the determination of Ni and Mn species in welding fumes, *Ann. Occup. Hyg.* 53 (2009) 333–340.
 - [46] J.M. Antonini, J.R. Roberts, D. Schwegler-Berry, R.R. Mercer, Comparative microscopic study of human and rat lungs after overexposure to welding fume, *Ann. Occup. Hyg.* 57 (2013) 1167–1179.
 - [47] D.M. Cate, P. Nanthasurasak, P. Riwalkulkajorn, C. L'Orange, C.S. Henry, J. Volckens, Rapid detection of transition metals in welding fumes using paper-based analytical devices, *Ann. Occup. Hyg.* 58 (2014) 413–423.
 - [48] N.B. Fethke, T.M. Peters, S. Leonard, M. Metwali, I.A. Mudunkotuwa, Reduction of biomechanical and welding fume exposures in stud welding, *Ann. Occup. Hyg.* 60 (2016) 387–401.
 - [49] H. Graczyk, N. Lewinski, J. Zhao, N. Concha-Lozano, M. Riediker, Characterization of tungsten inert gas (TIG) welding fume generated by apprentice welders, *Ann. Occup. Hyg.* 60 (2016) 205–219.
 - [50] K.W. Hanley, R. Andrews, S. Bertke, K. Ashley, Exploring manganese fractionation using a sequential extraction method to evaluate welders' gas metal arc welding exposures during heavy equipment manufacturing, *Ann Work Expo Health* 61 (2017) 123–134.
 - [51] D. Robertson, C. Thomas, S. Pratt, E. Lepel, V. Thomas, Low-level Radioactive Waste Classification, Characterization, and Assessment: Waste Streams and Neutron-Activated Metals, NUREG Report CR-6567, PNNL-11659, 2000.
 - [52] J.R. Davis, Alloying: Understanding the Basics, ASM international, 2001.
 - [53] C. Association, THE COPPER ADVANTAGE A Guide to Working with Copper and Copper Alloys, Copper Development Association, New York, 2013.
 - [54] J.R. Davis, K. Mills, S. Lampman, Metals handbook, in: Properties and Selection: Irons, Steels, and High-Performance Alloys, vol. 1, ASM International, Materials Park, Ohio 44073, USA, 1990, p. 1990, 1063.
 - [55] S. Saari, A. Arffman, J. Harra, T. Ronkko, J. Keskinen, Performance evaluation of the HR-ELPI plus inversion, *Aerosol. Sci. Technol.* 52 (2018) 1037–1047.
 - [56] ICRP, ICRP publication 68: dose coefficients for intakes of radionuclides by workers, *Ann. ICRP* (1994) 24.
 - [57] ICRP, ICRP Publication 66, Human respiratory tract model for radiological protection, *Ann. ICRP* (1994) 24.
 - [58] ICRP, ICRP publication 30 (Part 1): limits for intakes of radionuclides by workers, in: *Annals of the ICRP*, 1979.
 - [59] S. Guha, P. Hariharan, M.R. Myers, Enhancement of ICRP's lung deposition model for pathogenic bioaerosols, *Aerosol. Sci. Technol.* 48 (2014) 1226–1235.
 - [60] V.K.H. Bui, J.-Y. Moon, M. Chae, D. Park, Y.-C. Lee, Prediction of aerosol deposition in the human respiratory tract via computational models: a review with recent updates, *Atmosphere* 11 (2020) 137.
 - [61] T.C. Carvalho, J.I. Peters, R.O. Williams 3rd, Influence of particle size on regional lung deposition—what evidence is there? *Int. J. Pharm.* 406 (2011) 1–10.

- [62] W.C. Hinds, *Aerosol Technology: Properties, Behavior, and Measurement of Airborne Particles*, John Wiley & Sons, 2012.
- [63] V.I. Vishnyakov, S.A. Kiro, M.V. Oprya, O.D. Chursina, A.A. Ennan, Numerical and experimental study of the fume chemical composition in gas metal arc welding, *Aerosol Science and Engineering* 2 (2018) 109–117.
- [64] M.v. Smoluchowski, Versuch einer mathematischen Theorie der Koagulationskinetik kolloider Lösungen, *Z. Phys. Chem.* 92 (1918) 129–168.
- [65] J. Geng, H. Park, E. Sajo, Simulation of aerosol coagulation and deposition under multiple flow regimes with arbitrary computational precision, *Aerosol Sci. Technol.* 47 (2013) 530–542.
- [66] V.I. Vishnyakov, S.A. Kiro, A.A. Ennan, Formation of primary particles in welding fume, *J. Aerosol Sci.* 58 (2013) 9–16.
- [67] J. Kannosto, A. Virtanen, M. Lemmetty, J.M. Makela, J. Keskinen, H. Junninen, T. Hussein, P. Aalto, M. Kulmala, Mode resolved density of atmospheric aerosol particles, *Atmos. Chem. Phys.* 8 (2008) 5327–5337.
- [68] X.L. Wang, S. Barbanotti, J. Eschke, K. Jenssch, R. Klos, W. Maschmann, B. Petersen, O. Sawlanski, Thermal performance analysis and measurements of the prototype cryomodules of European XFEL accelerator - part I, *Nucl. Instrum. Methods A* 763 (2014) 701–710.
- [69] M. Levenson, K.D. Crowley, N.R. Council, *Research Reactor Aluminum Spent Fuel: Treatment Options for Disposal*, National Academies Press, 1998.
- [70] M. Hussain, P. Madl, A. Khan, Lung deposition predictions of airborne particles and the emergence of contemporary diseases, Part-I, *Health* 2 (2011) 51–59.
- [71] M.R. Bailey, E. Ansoborlo, R.A. Guilmette, F. Paquet, Updating the ICRP human respiratory tract model, *Radiat. Protect. Dosim.* 127 (2007) 31–34.
- [72] Y.S. Cheng, Mechanisms of pharmaceutical aerosol deposition in the respiratory tract, *AAPS PharmSciTech* 15 (2014) 630–640.
- [73] J. Klumpp, L. Bertelli, KDEP: a resource for calculating particle deposition in the respiratory tract, *Health Phys.* 113 (2017) 110–121.
- [74] T.B. Martonen, J.A. Rosati, K.K. Isaacs, Modeling deposition of inhaled particles, in: *Aerosols Handbook*, CRC Press, 2004, pp. 129–172.
- [75] K. Isaacs, J. Rosati, T. Martonen, L. Ruzer, N. Harley, *Modeling Deposition of Inhaled Particles*, *Aerosols Handbook*, CRC Press, Boca Raton, FL, 2012, pp. 83–128.
- [76] G. Bezemer, *Particle Deposition and Clearance from the Respiratory Tract*, 2009.
- [77] A.A. Rostami, Computational modeling of aerosol deposition in respiratory tract: a review, *Inhal. Toxicol.* 21 (2009) 262–290.
- [78] G. Oberdorster, E. Oberdorster, J. Oberdorster, Nanotoxicology: an emerging discipline evolving from studies of ultrafine particles, *Environ. Health Perspect.* 113 (2005) 823–839.
- [79] D.M. Brown, M.R. Wilson, W. MacNee, V. Stone, K. Donaldson, Size-dependent proinflammatory effects of ultrafine polystyrene particles: a role for surface area and oxidative stress in the enhanced activity of ultrafines, *Toxicol. Appl. Pharmacol.* 175 (2001) 191–199.
- [80] K. Donaldson, D. Brown, A. Clouter, R. Duffin, W. MacNee, L. Renwick, L. Tran, V. Stone, The pulmonary toxicology of ultrafine particles, *J. Aerosol Med.* 15 (2002) 213–220.
- [81] C.L. Tran, D. Buchanan, R.T. Cullen, A. Searl, A.D. Jones, K. Donaldson, Inhalation of poorly soluble particles. II. Influence of particle surface area on inflammation and clearance, *Inhal. Toxicol.* 12 (2000) 1113–1126.
- [82] G. Oberdorster, J. Ferin, G. Finkelstein, P. Wade, N. Corson, Increased pulmonary toxicity of ultrafine particles? II. Lung lavage studies, *J. Aerosol Sci.* 21 (1990) 384–387.
- [83] A.T. Saber, N.R. Jacobsen, P. Jackson, S.S. Poulsen, Z.O. Kyjovska, S. Halappanavar, C.L. Yauk, H. Wallin, U. Vogel, Particle-induced pulmonary acute phase response may be the causal link between particle inhalation and cardiovascular disease, *Wiley interdisciplinary reviews: Nanomedicine and nanobiotechnology* 6 (2014) 517–531.
- [84] H.M. Braakhuis, M.V.D.Z. Park, I. Gosens, W.H. De Jong, F.R. Cassee, Physicochemical characteristics of nanomaterials that affect pulmonary inflammation, *Part. Fibre Toxicol.* 11 (2014) 18.
- [85] P.H. McMurry, The history of condensation nucleus counters, *Aerosol Sci. Technol.* 33 (2000) 297–322.
- [86] M.R. Stolzenburg, P.H. McMurry, An ultrafine aerosol condensation nucleus counter, *Aerosol Sci. Technol.* 14 (1991) 48–65.
- [87] L.-E. Magnusson, J.A. Koropchak, M.P. Anisimov, V.M. Poznjakovskiy, J.F. de la Mora, Correlations for vapor nucleating critical embryo parameters, *J. Phys. Chem. Ref. Data* 32 (2003) 1387–1410.
- [88] P. Kulkarni, P.A. Baron, K. Willeke, *Aerosol Measurement: Principles, Techniques, and Applications*, John Wiley & Sons, 2011.